Received: Added at production | Revised: Added at production | Accepted: Added at production

DOI: xxx/xxxx

ARTICLE TYPE

Proof-of-concept of a robotic-driven photogrammetric scanner for intra-operative knee cartilage repair

Álvaro Bertelsen[1,2] | Amaia Iribar-Zabala[1] | Ekiñe Otegi-Alvaro[1] | Rafael Benito[1] | Karen López-Linares[1,2] | Iván Macía[1,2]

[1] Digital Health and Biomedical Applications area, Vicomtech Foundation, Basque Research and Technology Alliance (BRTA), Donostia-San Sebastián, Spain

[2] Bioengineering Area, Biodonostia Health Research Institute, Donostia-San Sebastián, Spain

Correspondence
Corresponding author Álvaro Bertelsen.
Email: abertelsen@vicomtech.org

Present address
Digital Health and Biomedical Applications area, Vicomtech Foundation, Basque Research and Technology Alliance (BRTA), Donostia-San Sebastián, Spain

Abstract

This work presents a proof-of-concept of a robotic-driven intra-operative scanner designed for knee cartilage lesion repair, part of a system for direct *in vivo* bioprinting. The proposed system is based on a photogrammetric pipeline, which reconstructs the cartilage and lesion surfaces from sets of photographs acquired by a robotic-handled endoscope, and produces 3D grafts for further printing path planning. A validation on a synthetic phantom is presented, showing that –despite the cartilage smooth and featureless surface– the current prototype can accurately reconstruct osteochondral lesions and their surroundings with mean error values of 0.199 ± 0.096 mm but with noticeable concentration on areas with poor lighting or low photographic coverage. The system can also accurately generate grafts for bioprinting, although with a slight tendency to underestimate the actual lesion sizes, producing grafts with coverage errors of -12.2 ± 3.7, -7.9 ± 4.9 and -15.2 ± 3.4 % for the medio-lateral, antero-posterior and craneo-caudal directions respectively. Improvements in lighting and acquisition for enhancing reconstruction accuracy are planned as future work, as well as integration into a complete bioprinting pipeline and validation with *ex vivo* phantoms.

KEYWORDS
intra-operative imaging, bioprinting, knee cartilage repair

1 | INTRODUCTION

Technological advances in medical robotics, regenerative medicine and material sciences may enable the repair of human tissue and organs employing direct three-dimensional (3D) bioprinting. A large amount of research on this subject has addressed the problem of scaffolding, although a few works have addressed *in vivo* or *in situ* approaches. Avoiding scaffolding is desirable, as it is time-consuming and increases the risk of contamination. However, direct 3D bioprinting requires the use of dexterous robotic manipulators –as linear gantry-type manipulators are unable to conform to the human body's curved surfaces– as well as accurate intra-operative scanning, specific path planning algorithms and appropriate formulations of bioinks.

A fundamental step for *in vivo* 3D bioprinting is accurate scanning of the target area. In the particular case of knee cartilage repair, pre-operative segmentation from magnetic resonance imaging (MRI) is the norm, although this imaging modality has limited resolution in the out-of-plane direction. Furthermore, multiple studies have also pointed out a systematic trend to underestimate the thickness of cartilage lesions using MRI: Krakowski et al. reported that MRI consistently underestimates the severity of cartilage lesions[1] and similar results were reported by independent studies by Zhang et al.[2], Campbell et al., –whose findings showed that MRI underestimated the size of 74% of their analysed chondral lesions, showing a mean area reduction of 1.04 cm^2 [3]– as well as Gomoll et al.[4].

Even if pre-operative diagnosis are available, it is agreed that chondral lesions must be assessed intra-operatively by means of arthroscopy, which is the method of choice specially for minimally-invasive approaches[5]. An automated touch-based scanner was developed by Lipskas et al.[6] –who proposed a dexterous manipulator for direct knee cartilage bioprinting– which used a probe

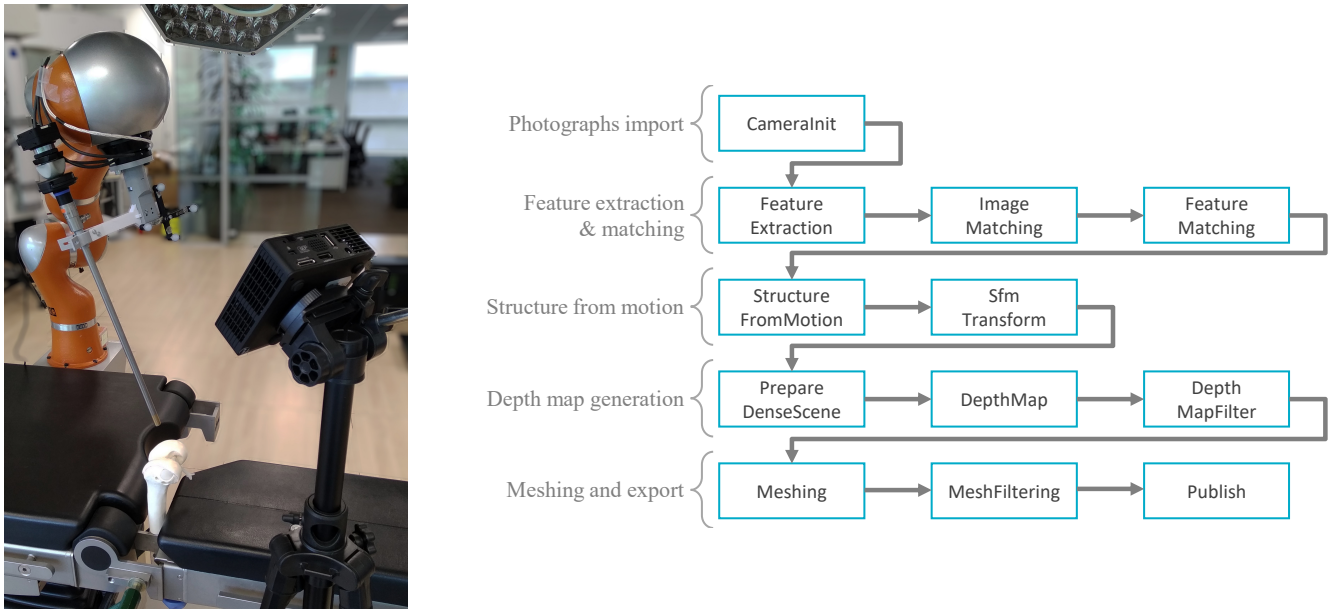

FIGURE 1 *Left:* Photograph of the proposed setup, including the robot-mounted endoscope, phantom and miniature projector. *Right:* schematic of the photogrammetric pipeline.

handled by a robotic arm. Their method offers good accuracy, although 3D point cloud formation required extended scanning time and limited resolution. In addition, touching of the knee cartilage increases risk of infection or unintended cartilage damage.

An appropriate alternative for osteochondral lesion scanning is offered by photogrammetry, that is, reconstruction of three-dimensional objects from sets of bi-dimensional photographs. The technique promises high accuracy while avoiding contact with the cartilague, yet it has received little attention: an early research led by Ronsky et al. on 1999 published the results of reconstruction of bone and cartilage regions using multiple cameras[7] and, afterwards, no further research has been found for these applications.

In this study, we propose the use of a 3D scanning method for osteochondral lesions employing photogrammetric techniques. This method offers high accuracy, high resolution, no contact and reduced scanning times. The proposed technology is well suited for *in vivo* three-dimensional bioprinting, offering easy to acquire and accurate reconstructions of lesions for posterior path planning and *in situ* repair.

2 | METHODS

2.1 | Setup

The proposed system consists of a collaborative robot (KUKA LWR 4+) which handles a custom-built tool that holds an endoscope coupled with a camera. The robot is able to pivot the endoscope around a femur phantom placed with its inferior axis (i.e. pointing from head to feet) facing up, simulating postures employed during open surgery. A separate fixed projector is also employed to project textured light over the cartilage and improve the performance of the photogrammetric algorithms. A picture of the complete setup is shown on Figure 1.

After manual initial positioning of the endoscope over the knee, the robot is able to pivot it, following a pre-defined trajectory and acquiring images during motion. After acquisition, the endoscope-camera pair can be decoupled from the robot's end-effector, replacing it with the extrusion tool needed for three-dimensional bioprinting.

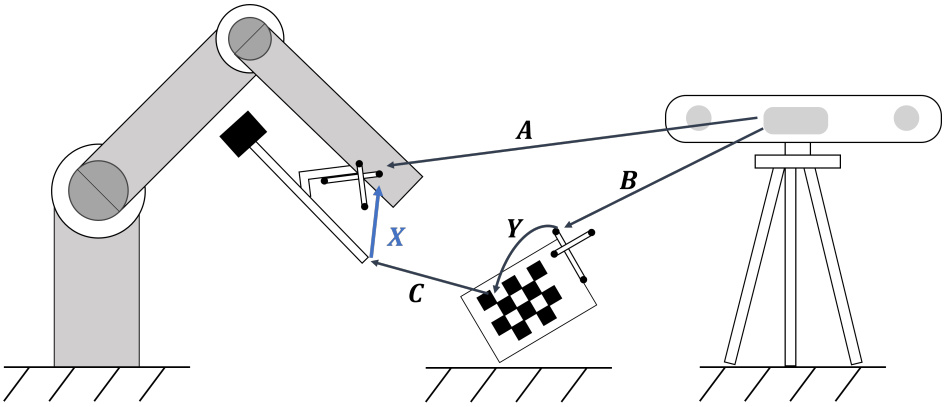

FIGURE 2 Graphical setup of the hand-eye calibration system, where X is the homogeneous transform matrix obtained as the result of the calibration; A and B are the homogeneous transform matrices given by the optical tracker; Y is a constant homogeneous transform matrix representing the pose of the tracker's markers with respect to the calibration board; and C is the homogeneous transform matrix of the board with respect to the endoscope obtained using *findChessboardCorners()* function of OpenCV library [10].

2.2 | Calibration

Direct printing over the cartilage's surface requires the calibration between the robot and the patient's coordinates, needed by the former to drive the extrusion tool and deposit bioink conforming to the tissue's curved surfaces. This is achieved by means of a hand-eye calibration between the endoscopic camera and the robot pose.

The hand-eye calibration was determined using the procedure proposed by Lee et al., which compares various methods, and suggests the best one in terms of accuracy and speed for clinical use [8]. The proposed setup is shown on Figure 2 and it is composed of a KUKA LWR4+ collaborative robot, equipped with a custom 3D-printed tool to hold the endoscopic system; a checkered calibration board with 15 mm-sided 5 by 4 pattern array, and an optical tracking system (Polaris Spectra, Northern Digital Inc) to track the markers attached to the board and endoscope. Prior to the hand-eye calibration, we conducted the camera calibration process using the widely known Zhang's method [9], employing 20 images with a resolution of 1280 by 1024 px.

Following the results stated by Lee et al. [8], calibration was performed keeping the robot in a fixed pose and pivoting the board around the endoscope's field of view, imaging 20 different poses. According to the authors, higher accuracy is achieved moving only the board and keeping the rest of equipment stationary, rather than the other way round.

In order to measure the accuracy of the hand-eye calibration, the back-projection error was calculated using 20 different poses not seen previously. On one hand, the ground truth calibration board's corners were obtained by means of image processing techniques from the OpenCV library [10]. On the other hand, we have calculated the extrinsic values of the camera with respect to the calibration board using the homogeneous transformation matrices X, A, B and Y –described on Figure 2–, aiming to project the points on the image and obtain the corners of the board. Both sets of 2D points per pose were then compared calculating the root mean square error.

2.3 | Photogrammetric pipeline

Surface and lesion scanning were implemented using the Meshroom application, based on the open-source AliceVision software library [11]. The full photogrammetric pipeline –schematised on Figure 1– has five large steps, the first being *photograph import,* where pictures are imported from the camera and associated with the corresponding set of intrinsic parameters, previously computed during the camera's calibration. Import is followed by *feature extraction and matching,* where feature points are detected on each photograph and matched across the full set of pictures, generating sets of neighbouring photographs and features. This step is followed by the *structure from motion* computation (SfM), in which a 3D point cloud with the most salient features is generated, as well as the cameras' 3D positions. The *depth map generation* follows, where all the photographs' pixels are back-projected into the 3D space, producing a dense dataset of depth values. Finally, the *meshing and export* step is executed to generate, filter and export the resulting surface as a triangle-based mesh.

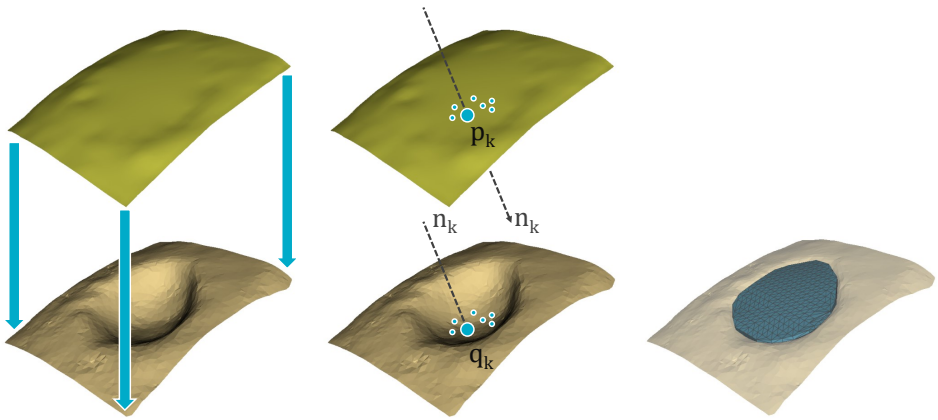

FIGURE 3 Graphical description of the graft generation: A rectangular patch is warped over the reconstructed lesion, fitting the outer margins but avoiding the centre (left). Then pairs of points are found tracing lines from the patch's points p_k along their normal vectors n_k, finding the corresponding points q_k over the lesion's surface (centre). Finally, a point cloud is produced joining the sets of p_k and q_k points, which is then meshed producing the graft's final surface (right).

For the image acquisition, we employed a miniature high-resolution camera (Teledyne FLIR Chameleon3 CM3-U3-13Y3C-S-BD) coupled with an endoscope (Olympus WA53000A), calibrated using the procedure described on Section 2.2.

Cartilage has a smooth and reflective surface which poses a considerable problem for the photogrammetric pipeline, in particular for the feature detection steps. To solve this, these surfaces were illuminated using a miniature projector (Optoma ML750E) that rendered an artificially textured pattern over them. The projected texture was formed by a 30 by 30 grid of ArUco markers [12], each one with a side length of 14 px, separation of 2 px and a 5 by 5 px code pattern taken from a pool of 1000 unique codes. Considering the device's projection distance of 550 mm, 1280 by 800 px matrix size, and the image's diagonal size of 430 mm, this yields a projected pixel size of 0.285 mm/px, a marker size of 3.988 mm and overall dimensions of the projected board of 136.17 by 136.17 mm, more than enough to cover the complete section of the femoral head, which has a width of approximately 78 mm, as shown on Figure 4. It must be noted that ArUcO markers were chosen as their texture patterns vary considerably between them –which is desirable for photogrammetric feature matching between image pairs– and that marker identification is never performed.

As photographs are ambiguous in scale, a reference object of known dimensions was placed in the scene to infer the objects' real dimensions. A ring-shaped object was fabricated with a set of CCTAG markers [13], arranged in known positions. The reference object was rigidly attached to the phantom, providing known pose and scale to the point cloud generated during the SfM step.

2.4 | Graft generation

Once the lesion surface was reconstructed, a second algorithm –implemented with the VTK software library [14]– was applied to generate an appropriate graft to fill the missing cartilage volume, as shown on Figure 3. First, a region of interest (ROI) was defined around the lesion and a rectangular-shaped patch –with dimensions equal to the ROI's width and length– was placed on the ROI's most inferior plane. The patch was registered to the lesion surface using an rigid iterative closest-point (ICP) algorithm [15] followed by a thin-plate spline transform. The latter was computed by pairs of corresponding points sampled on the rectangular patch's surface, finding their corresponding matches on the lesion's surface that intersected the lines traced by their normal vectors. To ensure a tight fit around the lesion area, all point pairs were included along 1 mm margins around the edges, but, inside the margins, pairs were only included if they were separated by less than 1 mm and the angles between their normal vectors were less than 10º. Once the patch was fitted, a similar sampling process was repeated to generate the graft's point cloud, sampling pairs of points found along the lines traced by the patch's vertex normal vectors, but only keeping points separated by 0.15 mm or more. Finally, a 3D Delaunay's triangulation algorithm was applied on the point cloud to produce the graft's mesh.

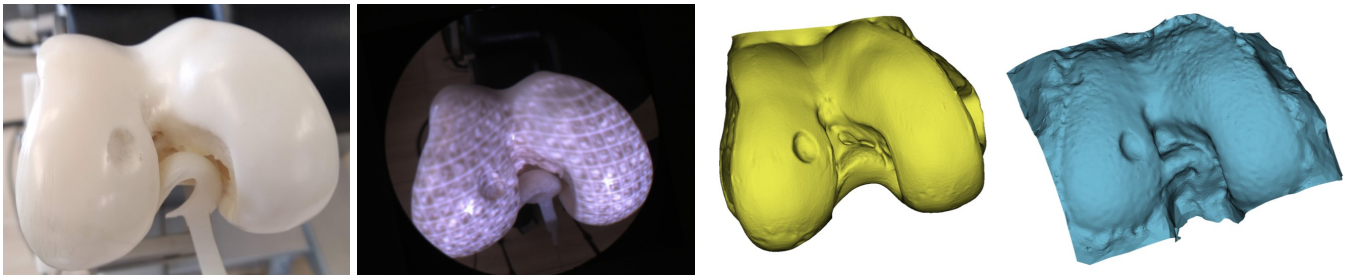

FIGURE 4 From left to right: photograph of the synthetic phantom with the milled lesion, acquired photograph of the same phantom illuminated with the projected textured pattern, reference high-resolution scan (yellow) and reconstruction obtained with the proposed method (blue).

2.5 | Phantom and evaluation metrics

A realistic synthetic phantom of a healthy knee (CLA-10, Coburger Lehrmittelanstalt) was used for validation. The phantom's femur was imaged using a high-resolution structured light scanner, and, afterwards, its cartilage was milled using a high-speed hand drill to simulate a common osteochondral lesion, with a circular shape with a 5 mm radius. After milling, the damaged femur was re-scanned to generate a second reference mesh. Both scans were then rigidly registered using the ICP algorithm and the lesion area was extracted from a ROI. Then, a reference graft model was produced using the algorithm described on Section 2.4, omitting the initial patch fitting. The generated model was kept as a reference for posterior evaluations.

Evaluations were made both on the *reconstructed lesion area* as well as for the *generated graft*. To evaluate the reconstructed lesion's mesh quality, it was initially registered to the reference scan using a rigid ICP transform, fitting the femoral inferior faces. Then, a ROI centred around the lesion was extracted and distances between the reconstructed mesh's vertices and their closest counterparts on the reference's faces were computed to obtain the meshes similarity. On the other hand, evaluations of the grafts were computed as comparisons with the reference graft's shape, in terms of bounding boxes dimensions, surface areas and enclosed volumes, as these indices are more relevant than per-vertex distances.

In order to evaluate the methods' performance, clinical benchmarks were also considered. Although there is little consensus for assessment of cartilage surface reconstruction –with most studies proposing qualitative measures–, more agreement exists for graft reconstruction, with Cohen et al. proposing the ± 1 mm range in the craneo-caudal direction as an acceptable metric for clinical research [16]. The same authors state that grafts that emerge up to 2 mm from the cartilage surface are acceptable, whereas depressed grafts may lead to unfavourable contact forces within the knee joint.

3 | DISCUSSION

3.1 | Hand-eye calibration

The homogeneous transformation matrix defining the camera pose was obtained using 20 different poses from the calibration plate, and validated on 20 additional unseen poses. The back-projection error obtained amounts to a mean of 15.04 mm with a standard deviation of ±5.01 mm, in pixels representing a 0.0068% of the total image pixels.

In a configuration similar to ours, Lee et al. [8] report a mean error of approximately 20 px, but with an image size of 720 by 576 px. This error is significant for the precision level required for *in situ* printing reconstruction of knee cartilage. To reduce this error, an option would be to get the endoscope closer to the calibration board, trying to avoid depth-associated inaccuracies. In addition, according to the literature [17], a wide distance between markers and markers-to-camera negatively affects the accuracy, and, therefore, a change in the endoscope's mounting may also be considered, bringing the tracker's markers closer to it.

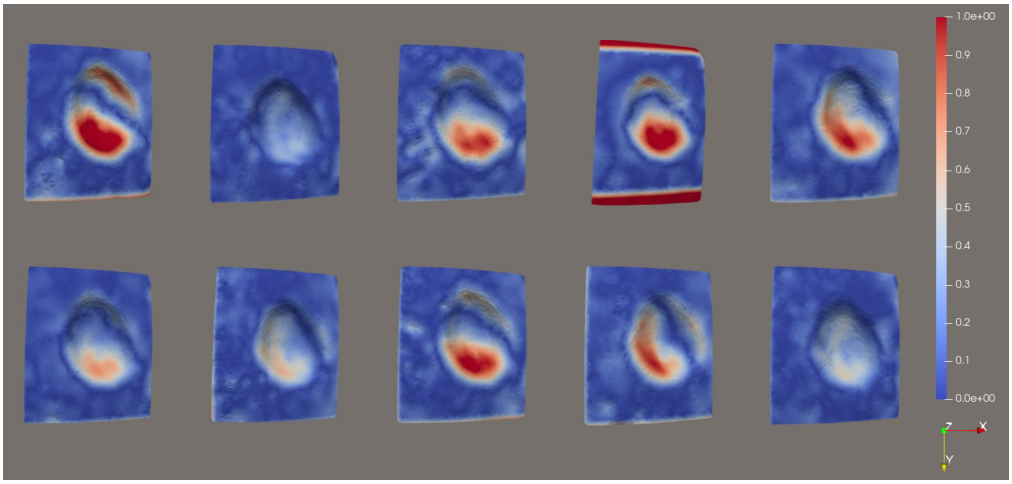

FIGURE 5 Visualisation of the surface reconstruction errors for all scans of the simulated lesion. Colour scale is given in the [0.0, 1.0] mm range. Analysis of the data reveals that reconstruction errors are focalised on the lesion's posterior (+Y) faces.

3.2 | Surface reconstruction

Ten scans of the simulated lesion were acquired, each one with 60 photographs acquired during one minute at a constant rate of 1 picture per second. A sample reconstruction –as well as pictures of the phantom and the reference scan– is shown on Figure 4. The reconstructed surfaces show a good agreement with the reference scan, depicting the lesion and the inferior plates of both femoral condyles. The medio-lateral and antero-posterior surfaces of the femur were reconstructed poorly, as the photographs had a limited coverage of these areas, intentionally left out as they are not relevant for the lesion reconstruction.

Mean surface reconstruction errors are reported on Table 1. An analysis of the data shows that the reconstruction method has an overall low euclidean error –0.199 ± 0.096 mm–, with a remarkably reduced inter-quartile range (IQR) of 0.074 mm. Errors along the medio-lateral and antero-posterior axes have reduced means and deviations –0.069 ± 0.023 mm and 0.085 ± 0.086 mm respectively–, as well as low median values and IQRs. Error along the craneo-caudal axis shows a mean with a slightly increased magnitude –0.125 ± 0.034 mm–, although its variability is quite reduced, with an IQR of only 0.045 mm. It is hypothesised that this increased error along this particular axis may be caused by its worse definition, as it matches the cameras' optical axes and is, thus, lost during photographic projection.

More detailed visualisation of reconstruction error across all acquisitions is shown on Figure 5. Analysis of the displayed surfaces reveal a clear pattern of error distribution, as it is not spread evenly across the whole ROI. Instead, it is focalised on the lesion's posterior face, where it reaches values greater than 1 mm, whereas it falls below 0.2 mm on most vertices outside the lesion. This localised distribution hints that the causes of error are deficiencies during acquisition, caused by an uneven illumination –which projected shadows on the rear part of the lesion– or an endoscope trajectory that failed to cover that particular region with a sufficient amount of photographs.

Photogrammetric pipelines were executed on a high-end laptop equipped with an Intel Core i7-7700 HQ processor, 16 GB of RAM and equipped with a Nvidia GeForce GTX 1070 GPU. Mean reconstruction times were of 14 ± 1 min, with a minimum of 13 min and a maximum of 16 min. As all scans had 60 photographs, mean reconstruction time per picture was of 14 sec/photo. Although these times can be considered reduced from a computer graphics point of view, they are still large for a surgical

Error	Mean ± dev	Median	IQR [Q1, Q3]	Range [min, max]
Euclidean	0.199 ± 0.096	0.195	0.074 [0.143, 0.217]	0.352 [0.078, 0.430]
Lateral	0.069 ± 0.023	0.075	0.033 [0.054, 0.087]	0.075 [0.023, 0.097]
Anteroposterior	0.085 ± 0.086	0.068	0.037 [0.042, 0.078]	0.299 [0.022, 0.320]
Craneocaudal	0.125 ± 0.034	0.133	0.045 [0.103, 0.148]	0.103 [0.065, 0.167]

TABLE 1 Summary of the lesion surface reconstruction errors, expressed as euclidean distances as well as projection onto the three axes. All values are given in mm.

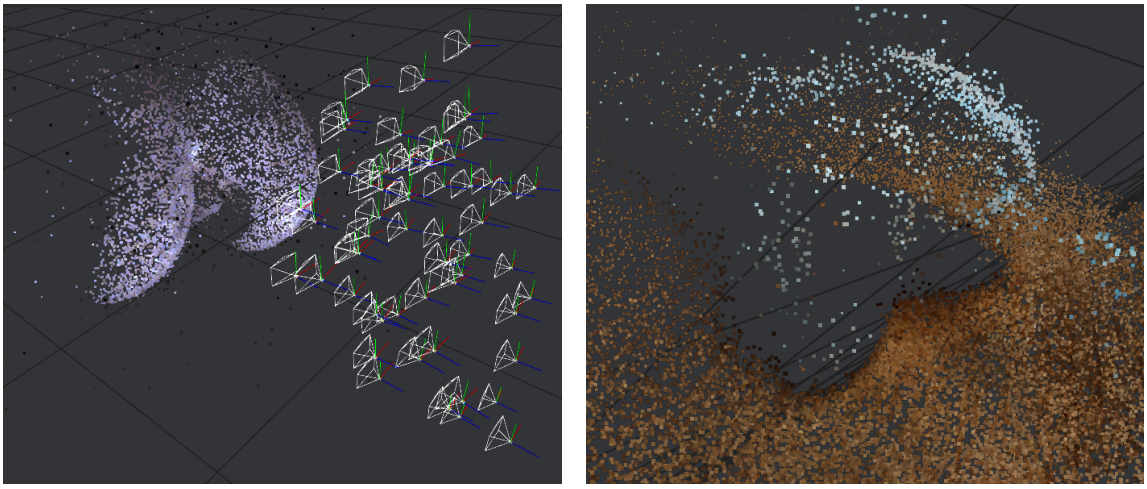

FIGURE 6 Sample point clouds generated by the SfM pipeline, with (left) and without (right) illumination with the marker texture. Note that the point cloud using markers has a clear and large coverage of the cartilage surface, whereas the other has so few triangulated points that becomes useless for mesh generation.

environment. However, there is room for improvement by optimisation of the acquisition trajectory and photogrammetric pipeline, by, for instance, reduction of the number of photographs, which should produce an approximately linear effect.

The identification of key frames during image acquisition, which has not been studied yet, could help to reduce reconstruction errors by removing images of poor quality which are producing noise, and instead focusing on scanning the positions which are more relevant for the reconstruction. In this sense, advantage could be taken of the use of the robotic device, whose position is always known. It could therefore be connected to the image acquisition device so that it only takes pictures in the positions in which these key frames are expected to be.

3.3 | Structure from Motion

An analysis of the structure from motion (SfM) steps was also made and its results are summarised on Table 2. This data show that the SfM pipeline was able to compute all camera poses on almost every case and that reconstructions had an average of 7456.9 ± 499.1 successfully triangulated points. Residual error –expressed as the root-mean-squared (RMS) re-projection error in pixel units– has an average value of 0.874 ± 0.036 px, showing a reduced an stable behaviour. Visual inspection of the results –such as the sample 3D point cloud shown on Figure 6– shows that the SfM pipeline is able to triangulate a large coverage of the cartilage surface, a result that confirms that the projected markers offer reliable features for extraction and matching. For the sake of completeness, Figure 6 also shows a case obtained with the same SfM pipeline, but without illumination with the projected markers. This case triangulated very few points over the cartilage surface, producing a result which is practically useless for depth mapping and meshing.

Value	Mean ± dev	Median	IQR [Q1, Q3]	Range [min, max]
# Photographs	59.5 ± 1.1	60	0 [60, 60]	3 [57, 60]
# Points	7456.9 ± 499.1	7509	796.8 [7082.8, 7879.5]	1358 [6678, 8036]
RMS error [px]	0.874 ± 0.036	0.874	0.053 [0.846, 0.899]	0.102 [0.825, 0.927]

TABLE 2 Summarised data of the SfM reconstructions, listing the numbers of successfully recovered camera poses, triangulated points and RMS error in pixels.

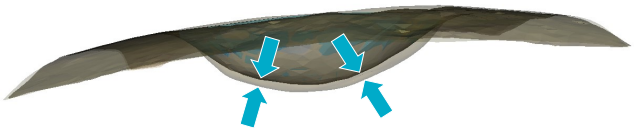

FIGURE 7 Sample reconstruction error: A reconstructed lesion model (opaque) is overlayed with the reference model (semi-transparent) showing a gap between them (marked with arrows). These reconstruction errors tend to appear on the lesions' bottoms, as these zones are more difficult to photograph during acquisitions.

3.4 | Graft generation

The analysis of the graft generation errors –reported on Table 3– reveals that the method has an appropriate accuracy, although with a slight tendency to underestimate the graft's size –and, thus, the lesion's– in terms of volume, surface area and dimensions along each of the three axes.

Analysis of the Table's data shows that errors along the medio-lateral and antero-posterior axes are larger than the ones observed on the craneo-caudal axis, both in terms of their absolute mean values and their deviations. Surprisingly, distributions are not isotropic: whereas the medio-lateral error has a larger mean and lower deviations —0.997 ± 0.306 mm–, the antero-posterior error shows a reduced mean but greater deviation —0.762 ± 0.472 mm–. The cause of this discrepancy remains unknown.

A negatively biased error is also observed in the craneo-caudal direction, although with lower mean and deviation values: -0.651 ± 0.145 mm. Visual analysis shows that the method accurately generates models that tightly match lesion's surrounding areas, but does not capture their full depths, as shown on Figure 7. In line with the effects described in Section 3.2, the cause of this error could be related to the coincidence of the craneo-caudal axis with the optical axes of the cameras, which leads to graphical data loss during photographic projection. This effect cannot be explained by mesh smoothing, as this step was disabled and the errors showed negligible changes. In all cases, no errors over 1 mm were observed in this direction.

Considering Cohen et al.'s [-1, 1] mm range in the craneo-caudal direction as a performance metric, we can see that the method obtains an acceptable result as the 100% points fall within this range. The authors also state that grafts that emerge up to 2 mm from the cartilage surface are acceptable, a result which is very improbable with the proposed method, as it tries to replicate the cartilage's original curvature. In fact, inclusion of an artificial offset may be needed to fully comply with this benchmark.

4 | CONCLUSIONS

In this work, we have investigated the feasibility of photogrammetric reconstruction of localised osteochondral lesions. This technology could be deployed as part of a robot-based, 3D bioprinting system for *in vivo* repair of knee cartilage, adaptable for other human tissues as well.

Error	Mean ± dev	Median	IQR [Q1, Q3]	Range [min, max]
Volume (mm^3)	-33.79 ± 6.25	-33.01	4.90 [-36.84, -31.95]	22.72 [-45.67, -22.95]
Area (mm^2)	-29.56 ± 7.20	-28.95	4.03 [-31.03, -27.00]	28.02 [-46.91, -18.89]
Dim LR (mm)	-0.997 ± 0.306	-0.931	0.170 [-1.006,-0.836]	1.080 [-1.828,-0.748]
Dim AP (mm)	-0.762 ± 0.472	-0.615	0.362 [-0.811,-0.449]	1.540 [-1.966,-0.426]
Dim IS (mm)	-0.651 ± 0.145	-0.618	0.092 [-0.657,-0.564]	0.476 [-0.971,-0.495]
Volume (%)	-35 ± 6.5	-34.2	5.1 [-38.2, -33.1]	23.6 [-47.4, -23.8]
Area (%)	-19.9 ± 4.8	-19.5	2.7 [-20.9, -18.2]	18.9 [-31.6, -12.7]
Dim LR (%)	-12.2 ± 3.7	-11.4	2.1 [-12.3, -10.2]	13.2 [-22.3, -9.1]
Dim AP (%)	-7.9 ± 4.9	-6.4	3.8 [-8.4, -4.7]	16 [-20.5, -4.4]
Dim IS (%)	-15.2 ± 3.4	-14.4	2.2 [-15.3, -13.1]	11.1 [-22.6, -11.5]

TABLE 3 Graft generation errors. Upper-half values are expressed in real world units (mm for lengths, mm^2 for areas and mm^3 for volumes), whereas lower-half values are expressed as percentages of the reference values. In all cases, negative values indicate lower measured values than the reference ones.

The proposed scanning method has been found capable of accurate reconstruction of cartilage lesion areas and generation of printable grafts. The method exhibits a remarkable accuracy in reconstruction of the lesion areas, with a mean euclidean error of 0.199 ± 0.096 mm. However, the method also showed a trend to produce inaccurate regions on the lesions' bottoms, probably due to inappropriate lighting or camera positions. For graft generation, the method showed an acceptable level of accuracy, although with a noticeable negative bias that translated into smaller grafts. A clinical benchmark was also considered, verifying that generated grafts' heights –in the craneo-caudal direction– fall within the ±1 mm acceptable range. Mitigation of the method's problems mentioned before may be obtained by improved lighting, enhanced acquisition trajectories –with improved lesion coverage– and inclusion of key-frame selection algorithms.

An experimental evaluation of a hand-eye calibration method was also reported in this work, although it did not reach the performance reported in the literature. Despite that this calibration is not strictly necessary for the photogrammetric reconstruction –as the latter is capable of computing the cameras' poses from the pictures–, it is needed for the posterior driving of the extrusion tool by the robot. Different enhancements will be sought in the future, such as more precise attachments of markers to calibration boards and alternative camera calibration algorithms, as the standard ones may not be appropriate for endoscopic vision. Finally, it is also feasible to incorporate the hand-eye calibration into the photogrammetric pipeline, adding the recorded robot poses during the SfM steps. It is also possible to self-calibrate the camera during the same process, approach that will also be explored.

The presented work has other shortcomings that should be addressed in the future: additional and more realistic validations should be made using *ex vivo* tissue and additional lesion sizes should be tested, covering the range of osteochondral lesions commonly found in clinical practice. Furthermore, the presented reconstruction method should be integrated in a complete pipeline, considering generation of bioprinting trajectories and generation of robotic trajectories to perform actual bioink extrusion. All these work lines are currently being addressed.

The proposed method assumes that the knee cartilage is exposed, as in open surgery approaches. Minimally-invasive approaches –by means of arthroscopy– were not considered, as these procedures require filling of the intra-articular space with liquid, which would dissolve the bioprinting gels during extrusion. In theory, the proposed method could be ported to do lesion scanning on arthroscopic procedures, although considerable improvements would be needed. In particular, texture projection into the intra-articular space, uneven lighting conditions and presence of floating debris would pose considerable challenges that would demand robust technological solutions.

Regenerative medicine employing *in situ*, three-dimensional, robotic-assisted bioprinting is demonstrated here and is a viable option for restoration of knee cartilage lesions. Further gains in regenerated tissue quality and reduction of post-operative complications would be considerable gains that justify further development of this technological line.

ACKNOWLEDGMENTS

This work has been funded by the Basque Government with Grant KK-2022/00019 under the ELKARTEK programme.

CONFLICT OF INTEREST

No potential conflict of interest were reported by the authors.

REFERENCES

1. Krakowski P, Karpiński R, Jojczuk M, Nogalska A, Jonak J. Knee MRI underestimates the grade of cartilage lesions. *Applied Sciences.* 2021;11(4):1552. doi: 10.3390/app11041552
2. Zhang M, Min Z, Rana N, Liu H. Accuracy of magnetic resonance imaging in grading knee chondral defects. *Arthroscopy: The Journal of Arthroscopic & Related Surgery.* 2013;29(2):349–356. doi: 10.1016/j.arthro.2012.04.138
3. Campbell A, Knopp M, Kolovich G, et al. Preoperative MRI underestimates articular cartilage defect size compared with findings at arthroscopic knee surgery. *The American journal of sports medicine.* 2013;41(3):590–595. doi: 10.1177/0363546512472044
4. Gomoll A, Yoshioka H, Watanabe A, Dunn J, T M. Preoperative Measurement of Cartilage Defects by MRI Underestimates Lesion Size. *Cartilage.* 2011;2(4):389–393. doi: 10.1177/1947603510397534
5. Friemert B, Oberländer Y, Schwarz W, et al. Diagnosis of chondral lesions of the knee joint: can MRI replace arthroscopy? A prospective study. *Knee Surgery, Sports Traumatology, Arthroscopy.* 2004;12(1):58–64. doi: 10.1007/s00167-003-0393-4
6. Lipskas J, Deep K, Yao W. Robotic-Assisted 3D Bio-printing for Repairing Bone and Cartilage Defects through a Minimally Invasive Approach. *Scientific Reports.* 2019;9:3746. doi: 10.1038/s41598-019-38972-2
7. Ronsky J, Boyd S, Lichti D, Chapman M, Salkauskas K. Precise measurement of cat patellofemoral joint surface geometry with multistation digital photogrammetry. *J Biomech Eng.* 1999;121(2):196–205. doi: 10.1115/1.2835104
8. Lee S, Lee H, Choi H, Jeon S, Hong J. Effective calibration of an endoscope to an optical tracking system for medical augmented reality. *Cogent Engineering.* 2017;4(1):1359955. doi: 10.1080/23311916.2017.1359955
9. Zhang Z. A flexible new technique for camera calibration. *IEEE Transactions on Pattern Analysis and Machine Intelligence.* 2000;22(11):1330-1334. doi: 10.1109/34.888718
10. Pulli K, Baksheev A, Kornyakov K, Eruhimov V. Real-time computer vision with OpenCV. *Communications of the ACM.* 2012;55(6):61–69. doi: 10.1145/2184319.2184337

11. Griwodz C, Gasparini S, Calvet L, et al. AliceVision Meshroom: An open-source 3D reconstruction pipeline.. In: 12th ACM Multimedia Systems Conference (MMSys 2021). ACM. Sep 2021; Istanbul, Turkey:241–247
12. Garrido-Jurado S, Muñoz-Salinas R, Madrid-Cuevas F, Medina-Carnicer R. Generation of fiducial marker dictionaries using mixed integer linear programming. *Pattern recognition.* 2016;51:481–491. doi: 10.1016/j.patcog.2015.09.023
13. Calvet L, Gurdjos P, Griwodz C, Gasparini S. Detection and accurate localization of circular fiducials under highly challenging conditions. In: Proceedings of the 2016 IEEE Conference on Computer Vision and Pattern Recognition (CVPR). IEEE. 2016:562–570
14. Schroeder W, Martin K, Lorensen W. *The visualization toolkit an object-oriented approach to 3D graphics*. Prentice-Hall, 1998.
15. Besl P, McKay N. A method for registration of 3-D shapes. *IEEE Transactions on Pattern Analysis and Machine Intelligence.* 1992;14(2):239–256. doi: 10.1109/34.121791
16. Cohen D, Lipton J, Bonassar L, Lipson H. Additive manufacturing for in situ repair of osteochondral defects. *Biofabrication.* 2010;2(3):035004. doi: 10.1088/1758-5082/2/3/035004
17. Schmidt J, Berg DR, Ploeg HL, Ploeg L. Precision, repeatability and accuracy of Optotrak® optical motion tracking systems. *International Journal of Experimental and Computational Biomechanics.* 2009;1:114. doi: 10.1504/IJECB.2009.022862